

AD-A067 899

DREXEL UNIV PHILADELPHIA PA DEPT OF MATERIALS ENGINEERING F/G 11/4
MICROSTRUCTURAL STABILITY AND STRENGTH OF THE CO,CR-(CR,CO)7C3 --ETC(U)
MAR 79 H SAATCHI, A LAWLEY

N00014-76-C-0205

NL

UNCLASSIFIED

1 OF 1

AD
A067899

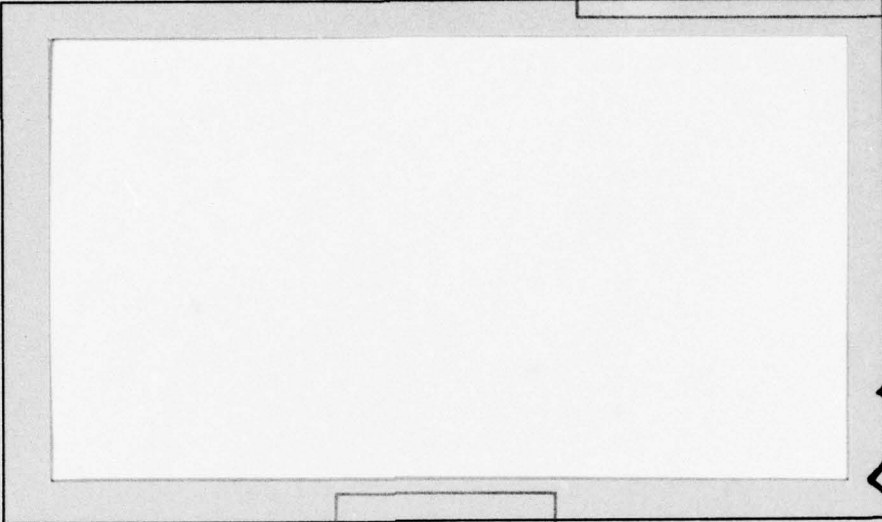


END
DATE
FILMED
6 --79
DDC

AD A 067899

LEVEL II

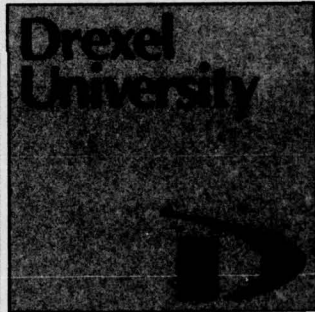
12



DDC FILE COPY

*See back page
for 1473*

DDC
APR 24 1979
R
CALIFORNIA



This document has been approved
for public release and sale; its
distribution is unlimited.

79 04 23 025

12

ADA067899

DDC FILE COPY

MICROSTRUCTURAL STABILITY AND STRENGTH OF THE
Co,Cr-(Cr,Co)₇C₃ IN-SITU COMPOSITE

H. Saatchi and A. Lawley

March 1979

Technical Report

Office of Naval Research
Arlington, Virginia 22217

Contract #N00014-76-C-0205

Reproduction in whole or in part is permitted
for any purpose of the United States Government

Distribution of this document is unlimited

Drexel University
Department of Materials Engineering
Philadelphia, Pa. 19104

79 04 23 025



Introduction

The increase in efficiency of a gas turbine engine with increasing inlet temperatures has led to the consideration of in-situ metal matrix composites for use as a blade material (1,2). Primary interest is vested in three classes of eutectic alloy compositions, namely: Ni or Co alloy matrices reinforced with a rod-like monocarbide; Co-Cr matrix compositions reinforced with rod-like M_7C_3 type carbides; $\gamma/\gamma'-\delta$ consisting of Ni_3Nb (δ) lamellae and precipitates of Ni_3Al (γ') in the Ni alloy matrix (γ). These reflect enhanced high-temperature stiffness and strength over conventional superalloys. Recent reviews by Lawley (3) and Stoloff (4) provide detailed comparisons of mechanical behavior and an assessment of the current level of understanding of microstructure-mechanical property relationships in the above systems.

Intrinsically, in-situ composites are stable at elevated temperatures, a characteristic derived from their solidification under near equilibrium conditions, coupled with low-energy interface boundaries (5). However, microstructural instability and attendant property changes may occur as a result of prolonged high temperature exposure or thermal cycling excursions (6). Thus, coarsening can take place by two-dimensional Ostwald ripening (7-9) and by the migration and annihilation of growth faults (8,10,11). Physical and chemical characteristics that influence the cyclic stability of eutectic composites are thermal expansion mismatch, mutual solubility of phases with temperature, surface energy of the reinforcing phase, perfection of the reinforcing phase and the existence of allotropic transformations (12). The severity of the thermal cycle is a function of temperature range ΔT , maximum temperature T_{max} , heating and cooling rates and hold time at T_{max} .

In several studies, the effect of thermal cycling on the microstructure and strength of monocarbide-reinforced (12,13-21) and $\gamma/\gamma'-\delta$ (12,13,22) high temperature in-situ composites has been examined. These confirm sensitivity

to the form of the cyclic temperature-time profile and suggest that in general, delta-reinforced nickel alloys (γ - δ , γ/γ' - δ) exhibit greater stability re thermal cycling than monocarbide-reinforced cobalt or nickel alloys. In the latter, the carbide develops serrations during cycling and this can result in an increase or decrease in strength depending on the alloy and cycling conditions (14,20,21).

The purpose of the present study has been to examine the effects of isothermal exposure and thermal cycling on the microstructural stability and strength of the $\text{Co,Cr-(Cr,Co)}_7\text{C}_3$ in-situ composite. This composite is formed by a monovariant ternary reaction and contains 30% by volume of aligned fibers in a cobalt-rich matrix (23). The nature of the constituents suggest that the alloy might be useful as an elevated temperature structural material; in the as-grown condition, the composite exhibits high strength and creep resistance but limited ductility (24). Concurrent studies by Lawley et al. on this system have identified microstructure-property relations for toughness (25,26) and resistance to fatigue crack propagation (27).

Experimental Procedure

A. Composite Preparation

Master alloy rods were prepared from 99.99% purity Co and Cr and spectrographic grade C by induction melting in an aluminum crucible under argon and casting in a stainless steel mold. The overall composition of the alloy was Co-41% Cr-2.4% C by weight. Ingots 12.7 mm dia. and \sim 250 mm in length were then prepared by directional solidification of the master alloy rods in high purity alumina tubes under a dynamic argon atmosphere. The induction furnace was a modified version of the design developed by Thompson et al. (28) and is illustrated schematically in Figure 1. By using a susceptor with a conical profile and a linear spiral coil with a pancake at the base, axial thermal gradients (G) $\sim 1.1 \times 10^5$ C/m were achieved at the

liquid-solid interface (29). For a growth rate (R) of 5×10^{-6} m/s the attendant G/R was 220×10^8 °Cs/m². This resulted in an aligned rod-like reinforcement of (Cr,Co)₇C₃ in a cobalt-rich matrix at a volume fraction $V_f = 0.3$.

B. Post Solidification Treatments

(a) Isothermal Exposure

The directionally solidified bars were sectioned into 25.4 mm lengths and sealed in quartz capsules under argon. Isothermal exposure was carried out at temperatures of 913°C, 1121°C and 1242°C for periods up to 44×10^5 s; these correspond to matrix homologous temperatures of $0.76 T_m$, $0.89 T_m$ and $0.97 T_m$ respectively.

(b) Thermal Cycling

Thermal cycling regimes studied were: 357°C to 913°C, 746°C to 913°C and 538°C to 1121°C, up to 10^4 cycles; these provided different values of T_{max} and $\Delta T (= T_{max} - T_{min})$. In addition, a hold time of 480s was incorporated at T_{max} and T_{min} for the 746°C to 913°C cycle, and a 3360s hold time at T_{max} only for the 538°C to 1121°C cycle.

Specimens for thermal cycling were placed in a quartz tube under flowing argon and located along the focal axis of a radiant heat reflector furnace. Details of the thermal cycling facility, including the provision for hold times, are given elsewhere (29). Heating and cooling curves (no hold time) for one cycle between 357°C and 913°C and between 746°C and 913°C, are shown in Figures 2(a) and 2(b). The corresponding curve for the 538°C to 1121°C cycle is shown in Figure 3. Actual time-temperature profiles for thermal cycling involving a hold-time are shown in Figures 4 and 5; the total elapsed times per cycle were 1050s and 3690s respectively.

C. Mechanical Testing

Mechanical testing was performed at ambient and elevated temperatures up to 1121°C on longitudinal and transverse orientation specimens in the as-grown condition, and following post-solidification heat-treatments. Specimens 4 mm x 4 mm x 8 mm long were sliced from the directionally solidified ingots and each surface wet ground and polished. End faces were parallel to within 8.725×10^{-7} radians. Initial and final specimen dimensions were measured by a precision micrometer to within 0.00127 mm.

For testing at temperatures below 913°C, the platens of the compression facility were made from Kennometal alloy K68. Above this temperature, high density recrystallized alumina was used. Specimens were induction heated using a graphite susceptor and protected in flowing argon. Details of the facility are given elsewhere (29).

D. Metallography

Microstructures and fracture morphologies of the composites were characterized by a combination of optical microscopy and scanning and transmission electron microscopy. For optical metallography, specimens were wet ground through 600 grit paper, rough polished with diamond paste and given a final vibratory polish using Linde A and B alumina. Polished surfaces were either lightly etched in aqua regia or deep etched in boiling aqua regia to partially remove the matrix.

Scanning electron microscopy was used to examine the deep etched composites and fracture surfaces. Constituents in the microstructures were identified by means of energy-dispersive x-ray point analysis. Extracted fibers and precipitates were examined in the transmission electron microscope.

Results

A. Microstructures

(a) As-Grown

Representative optical micrographs in the transverse and longitudinal orientations are illustrated in Figures 6(a) and 6(b). Though aligned, the fibrous reinforcement exhibits irregularities in cross-section, branches and serrations. Faceting of fiber cross-sections is evident in Figure 6(a) and is further illustrated by scanning electron microscopy after deep etching of the matrix, Figure 6(c); this also reveals the hexagonal symmetry of the reinforcement. Similar microstructures have been reported by Thompson and Lemkey (23) in composites grown at a similar rate. The inter-fiber spacing (λ) was $\sim 4\mu\text{m}$.

More detail on reinforcement morphology is provided from an examination of extracted fibers, Figures 7 and 8. Representative energy-dispersive x-ray point analysis for the matrix and fiber are shown in Figure 9. Two traces are given for the fiber, one corresponding to the center of the fiber (fc) and the other to the fiber surface (fs) in the region of the serrations. As seen in Figure 9, the Co content is different in the two locations, being lower in the body of the fiber than at the fiber surface.

(b) Isothermal Exposure

At 913°C precipitation occurs in the matrix, Figure 10 (a), (b) and (c). This enhances the irregularities in cross section of the reinforcing fibers, as seen in the longitudinal orientation micrographs. Compared to the as-grown condition (Figure 6), the fibers are more rounded and have broken up into shorter lengths. Following exposure at 913°C , one composite was taken to 1121°C for 6.3×10^4 s. This resulted in a dissolution of the precipitate, Figure 10(d).

Corresponding scanning electron micrographs for the three times of exposure at 913°C are given in Figure 11. Initially the precipitates approximate a plate-like morphology, Figure 11(a); this changes to a more cylindrical form with secondary arms developing on the precipitates at longer times (Figure 11(b)). Finally the precipitates become more spherical and coalesce, Figure 11(c). These micrographs show clearly the perturbations in cross-section and shape of the main fibers that develop as a result of the formation of the precipitate. Transmission electron microscopy after exposure at 913°C further illustrates the highly irregular surface profile of the fibers associated with the precipitation process, Figure 12. Energy-dispersive x-ray point analyses of the matrix, fiber and precipitate are compared in Figure 13. These show that the precipitate is richer in Co than the main fibers.

Isothermal exposure at 1121°C and 1242°C leads to a rounding of fiber cross-sections, cf. Figures 14 and 6(a). Precipitates do not form in the matrix, in contrast to the response observed at 913°C, cf. Figures 14 and 10(a), (b), (c). After isothermal exposure at these high homologous temperatures, the fiber surfaces appear smoother than in the as-grown condition, Figure 15. Surface irregularities (serrations) on the fibers of the type present in the as-grown composites (Figure 8) were not observed after exposure at 1121°C or 1242°C. Changes occur in the distribution of the Co in the composite, compared to the as-grown condition, cf. Figures 16 and 9. After isothermal exposure at either temperature, the Co content in the body of the fibers is lowered, but is increased in the outer regions of the fibers, i.e. adjacent to the cobalt-rich matrix.

(c) Thermal Cycling

Thermal cycling over the range 357°C to 913°C leads to changes in microstructure and fiber morphology. The surface irregularities characteristic

of the as-grown condition are intensified and this is accompanied by precipitation in the matrix. Degradation of the fiber surface condition increases with increasing numbers of thermal cycles. Examples of these changes are given in Figures 17 and 18. The highly serrated fiber surface profile is clearly seen after 7000 cycles in the scanning electron micrograph of Figure 18. Some rounding of fiber cross-sections also occurs during thermal cycling.

Energy-dispersive x-ray analysis shows that the thermal cycling gives rise to changes in the cobalt distribution similar to those occurring during isothermal exposure at 913°C. Thus, the precipitates have a different composition (higher Co level) than the main fibers, and the Co level in the center of the fibers is lower than that in the outer fiber surfaces.

Microstructural changes occurring as a result of thermal cycling between 538°C and 1121°C resemble those described above for isothermal exposure at 1121°C. Thus, smooth fiber surfaces develop and there is a rounding of the fiber cross-sections. There is one important difference, namely that a small amount of fine-scale precipitate develops in the matrix after thermal cycling for ≥ 5000 cycles. Energy-dispersive x-ray analysis again confirms a higher Co level at the fiber surfaces than in the fiber interior, and that the precipitate has a similar Co level to that at the fiber surfaces.

Thermal cycling between 746°C and 913°C with a 480s hold time at T_{\max} and T_{\min} leads to the formation of precipitates in the matrix, Figure 19. The precipitates are roughly spherical in shape with diameters in the approximate range 0.01 μm to 0.9 μm . Precipitation is accompanied by a general degradation of the fiber reinforcement, as reflected in highly irregular fiber shapes/diameters, Figures 19 and 20. Thus, serrations and necks are common features of the carbide morphology after this regime of thermal cycling. Again, energy-dispersive x-ray analysis confirms a higher Co level in the precipitates and outer fiber regions than in the center of the fibers.

Thermal cycling between 538°C and 1121°C with a hold time of 3360s at T_{\max} causes severe microstructural damage. This takes the form of fiber rounding, a break up of fibers into shorter lengths of irregular diameter, and void formation at fiber-matrix interfaces. These changes are illustrated in Figures 21 and 22. The voids coalesce into holes several microns in diameter. Precipitates are not observed in the matrix but the Co level in the outer fiber regions is higher than in the center of the fibers.

B. Compressive Strength

(a) As-Grown

Typical engineering stress-engineering strain curves in compression at room temperature for the longitudinal (stress parallel to fibers) and transverse (stress perpendicular to fibers) orientations are illustrated in Figure 23. The ultimate compressive strengths in the longitudinal ($\sigma_{UC,L}$) and transverse ($\sigma_{UC,T}$) orientations are 2358 MPa and 1779 MPa, respectively; strains to failure are in the range 0.03 to 0.04. Temperature dependence of strength in both orientations is shown in Figure 24; in both cases there is a relatively sharp decrease in strength above ~600°C.

(b) Isothermal Exposure

Isothermal treatment at 913°C results in a significant increase in strength, Figure 25. From this figure it is seen that subsequent treatment at 1121°C leads to a decrease in strength; however, $\sigma_{UC,L}$ is still ~11% higher than in the as-grown composite. In contrast to the above, only small increases in $\sigma_{UC,L}$ and $\sigma_{UC,T}$ are observed following isothermal exposure at 1121°C, Figure 26.

(c) Thermal Cycling

The two thermal cycling regimes (357°C to 913°C and 538°C to 1121°C) without hold time promote increases in $\sigma_{UC,L}$ and $\sigma_{UC,T}$. Strength variations, as a function of the number of thermal cycles, are plotted in Figures 27 and 28.

Thermal cycling between 746°C and 913°C with a hold time at T_{max} and T_{min} also promotes strengthening. For example, after 1000 cycles, $\sigma_{UC,L}$ and $\sigma_{UC,T}$ are 32% and 57% higher than in the as-grown condition. In contrast, thermal cycling between 538°C and 1121°C with a hold time at T_{max} leads to an initial increase in strength followed by a decrease, Figure 29. After 1200 cycles both $\sigma_{UC,L}$ and $\sigma_{UC,T}$ are lower than the corresponding strength levels in the as-grown condition.

C. Fracture

For all composite conditions examined, compression at room temperature leads to an overall plane of fracture inclined at approximately 45° to the load axis; this applies to both orientations. Fracture is accompanied by extensive matrix shear and transverse cleavage of the fiber reinforcement, Figure 30. Secondary cracks are evident in the vicinity of the fracture surfaces.

When compressive loading is applied above the ductile to brittle transition temperature of the reinforcing fibers (~600°C) both constituents exhibit plastic flow. Examples are given in Figure 31. The intense bands of shear give rise to fiber buckling and fragmentation. The presence of kink bands is a further indication of elastic fiber buckling. For deformation at 929°C, debonding does not occur at fiber-matrix interfaces, Figure 31; this is a reflection of the excellent bond integrity characteristic of in-situ composites. Compressive deformation at 1121°C is accompanied by dynamic recovery in the matrix. In the longitudinal orientation, interface delamination now occurs.

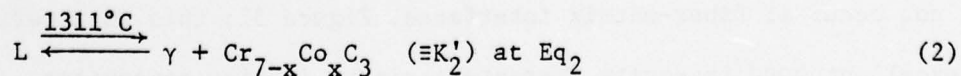
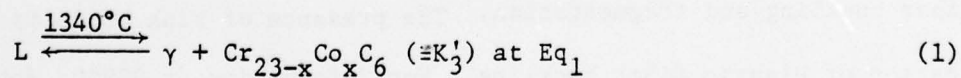
Discussion

A. Microstructures

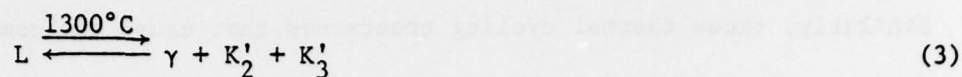
(a) As-Grown

In the as-grown condition, the composite of overall composition Co-41%Cr-2.4%C is essentially quasibinary in nature with the conjugate solid phases being the solid solution cobalt-rich matrix and solid solution carbide based on $\text{Cr}_{7-x}\text{Co}_x\text{C}_3$ ($\equiv \text{K}'_2$). The pertinent section of the liquidus surface in the Co-rich corner (23,30) is shown in Figure 32 with the alloy composition at Eq_2 . However, the observed carbide morphologies and associated energy-dispersive x-ray diffraction traces suggest the presence of more than one carbide. In particular, small branches are observed on the main fibers (Figure 8) with the Co content lower in the center of the main fibers than in these branches. Further, the outer layers of the main fibers exhibit lower Co levels than in the interior of the fibers.

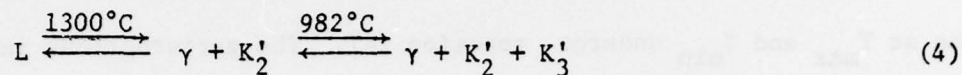
Sahm et al. (31) and Köster and Sperner (30) have considered possible reactions occurring during cooling of the ternary alloy. A section along the eutectic trough (30,31) is illustrated in Figure 33; this is similar to a more recent section reported by Perry et al. (32). In this figure the solid lines refer to the work of Sahm et al. and the dashed lines to that of Köster and Sperner. There are two pseudobinary regions Eq_1 and Eq_2 located between the ternary eutectics $\text{E}_{\text{T}1}$ and $\text{E}_{\text{T}2}$. The associated quasieutectic reactions are:



Köster and Sperner also proposed the ternary reaction at S:



A further possible reaction at Eq₂ is:



Evidence for reaction (4) has been reported by Thompson and Lemkey (23). It is believed that this reaction occurred in the present study. As shown in Figure 33, the solidus boundary dividing the two-phase $\gamma + K_2'$ region from the three-phase $\gamma + K_2' + K_3'$ region is extremely temperature-dependent. Depending on the exact location of this line relative to Eq₂, the reaction (4) could occur on cooling. If this is so, then in the as-grown composite, the outer regions of the main fibers and the small branches are the K_3' carbide while the fiber center has the composition of the K_2' carbide.

(b) Post-Solidification Heat Treatment

Microstructural changes accompanying post-solidification heat-treatment are consistent with the conclusions arrived at in the previous section. Thus, isothermal exposure at 1121°C and 1242°C stabilizes the two-phase $\gamma + K_2'$ structure. In contrast, at 913°C reaction (4) takes place and K_3' is precipitated out into the matrix between the fibers of K_2' . These precipitates are nucleated at the fiber surfaces, grow into the matrix and finally pinch-off from the main fiber, as illustrated in Figure 34. The subsequent disappearance of the K_3' precipitate at 1121°C after its formation at 913°C lends credibility to reaction (4). Scarlin (33) has reported that in this composite after 10.8×10^5 s at 950°C, the M_7C_3 carbide is completely transformed into the $M_{23}C_6$ form.

Similarly, those thermal cycling treatments that cause the composite to spend a prolonged time in the approximate temperature range 760°C to 982°C result in the formation of the K_3' precipitate along with K_2' and the Co-rich matrix. Thus, composites thermally cycled between 746°C and 913°C with a hold time at T_{\max} and T_{\min} undergo reaction (4). The perturbations in cross-section left after precipitates pinch-off are the sites for subsequent break-up of the main fibers into shorter lengths.

The most pronounced effect of the precipitation-dissolution sequence is seen on thermal cycling between 538°C and 1121°C with a hold time of 3.36×10^6 s at T_{\max} . The $M_{23}C_6$ -type carbide is precipitated in the range 760°C to 982°C but is dissolved during the hold time at T_{\max} (1121°C). Microvoids which subsequently coalesce are attributed to the dissolution process. In the case of thermal cycling without hold time, the composite spends a limited time in the critical temperature range required for precipitation and dissolution; this gives rise to partial decomposition and a fine-scale precipitate.

Spheroidization of the K_3' precipitate and the rounding of fiber cross-sections occur in order to minimize interphase interfacial area. Similarly, after fibers break up into shorter lengths these become more rounded under the driving force of interface surface energy; this is seen clearly in the longitudinal section micrographs of Figures 10, 19 and 21.

Growth of the branches out from the main fibers into the matrix, as a first step in the formation of K_3' , will have the effect of increasing the fiber density. Thus, in transverse cross-sections, the number of fibers per unit area will increase. A more subtle manifestation of microstructural change accompanying either form of post-solidification heat treatment is fiber splitting. Fiber cross-sections in the as-grown condition are highly irregular (Figure 6a) with reentrant angles and on isothermal exposure

or thermal cycling, some of these fibers break up or split longitudinally. The effect is best seen in scanning electron micrographs of deep-etched specimens, for example Figures 15, 22 and 35. This phenomenon, which increases fiber density, occurs whether or not the conditions of isothermal exposure or thermal cycling promote formation of the K_3' precipitate.

The various changes in microstructure brought about by the different regimes of isothermal exposure and thermal cycling are summarized in Table I. Associated strength modifications are also included.

B. Strength and Microstructure

Room temperature strength levels at fracture in the as-grown condition are higher than those reported by Thompson et al. (24) and Koss and Copley (34). $\sigma_{UC,L}$ is 2358 MPa compared to 1894 MPa, and $\sigma_{UC,T}$ is 1779 MPa compared to 1357 MPa. Since growth rates were similar the difference is attributed to the higher thermal gradient (and hence G/R) achieved during directional solidification in the present study.

For failure by buckling in the 'shear-mode' of a composite consisting of elastic fibers and plastic matrix, $\sigma_{UC,L}$ is given by (35):

$$\sigma_{UC,L} = \left[\frac{V_f E_f \sigma_m^Y}{3(1-V_f)} \right]^{1/2} \quad (5)$$

where

- $\sigma_{UC,L}$ = ultimate compressive strength of the composite
- V_f = volume fraction of reinforcement
- E_f = modulus of elasticity of the fiber
- σ_m^Y = yield strength of the matrix.

Using experimentally determined values for the elastic modulus of the fiber [$E_f = 29.6 \times 10^4$ MPa, (24)] and for the yield stress of the matrix [$\sigma_m^Y = 151.6$ MPa, (36)], and with $V_f = 0.3$, equation (5) gives:

$$\sigma_{UC,L} = 2538.8 \text{ MPa}$$

This is within 7% of the measured value of 2358 MPa in the as-grown condition. The sharp drop in compressive strength at temperatures $\geq 600^\circ\text{C}$ is the result of plastic deformation of the reinforcing phase above the ductile-to-brittle transition temperature.

The changes in compressive strength caused by isothermal exposure or thermal cycling are now considered in light of the accompanying composite microstructure. Precipitation of the K_3' carbide in the matrix is expected to increase strength since matrix dislocation motion will be impeded. The extent of the effect will be a function of the shape and degree of coherency of the precipitate. Similarly fiber splitting, with an associated increase in fiber density, should enhance strength. Fiber break-up into shorter lengths and the accompanying spheroidization will decrease strength relative to the as-grown condition since the reinforcement is no longer continuous. Microvoids associated with the dissolution of K_3' during thermal cycling will also cause a strength decrease. A further effect arises from the allotropic transformation of the Co-rich matrix at $\sim 820^\circ\text{C}$ with an accompanying increase in the concentration of point defects.

For incoherent precipitates, the Orowan-Ashby model of dispersion hardening (37) gives a strength increment $\Delta\sigma_{dh}$ of:

$$\Delta\sigma_{dh} = \frac{0.13 \bar{b} G_m}{\bar{l}} \ln \left(\frac{r}{\bar{b}} \right) \quad (5)$$

where \bar{b} = Burgers vector

r = precipitate ($\equiv K_3'$) radius

\bar{l} = spacing between precipitates

G_m = shear modulus.

For the isothermal and thermal cycling treatments which promote precipitation of K_3' , accompanying strength increases are in the range 500-750 MPa. In terms of equation (5), this would require values of $\bar{l} \sim 200\text{\AA} - 300\text{\AA}$ ($0.02\mu\text{m} - 0.03\mu\text{m}$). A detailed transmission electron microscope examination would be required to establish \bar{l} (and \bar{r}); however, the calculated \bar{l} , in the range $200\text{\AA} - 300\text{\AA}$, seems reasonable.

Quantitatively, the effect of fiber splitting on strength can be analyzed by means of a modified Hall-Petch model (38,39). Assuming that the fibers in the composite act as barriers to slip analogous to grain boundaries, the grain diameter in the Hall-Petch equation is replaced by the average interfiber spacing $\bar{\lambda}$. Any decrease in $\bar{\lambda}$ as a result of fiber splitting will lead to a strength increase. It was not the intent in this study to make a detailed evaluation of λ as a function of post-solidification heat-treatment. However, in a concurrent study (40), the normal pattern of fiber coarsening (with an accompanying increase in λ) was observed so that this would outweigh any local-scale decreases in λ due to fiber splitting. It can therefore be concluded that small, if any, increases in strength are attributable to fiber splitting. The average strength decrement due to longitudinal fiber break-up is also difficult to calculate.

Conclusions

1. Significant changes in composite microstructure can accompany elevated-temperature isothermal exposure and thermal cycling in $(\text{Co,Cr})-(\text{Co,Cr})_7\text{C}_3$.
2. Changes in strength are caused by: precipitation and dissolution of K_3' in the cobalt-base matrix, fiber rounding and splitting, spheroidization of K_3' and/or the primary reinforcing phase K_2' and void formation at matrix-fiber interfaces.

3. The Orowan-Ashby model of dispersion hardening provides a reasonable estimate of the observed strength enhancement due to the presence of K_3' carbide precipitates.
4. Below the ductile-to-brittle temperature of the reinforcing phase, compressive loading promotes ductile shear of the matrix and transverse cleavage of fibers; failure occurs via the in-phase buckling mode.
5. Above the ductile-to-brittle temperature both matrix and reinforcement deform plastically; shear bands and fiber break-up accompany fiber buckling.

References

1. L. P. Jahnke and C. A. Bruch, Specialists Meeting on Directionally Solidified In-Situ Composites, Editors: E. R. Thompson and P. R. Sahm, AGARD Conf. Proc. #156, Technical Editing and Reproduction Ltd., London, 1974, p. 3.
2. M. F. Henry, M. R. Jackson and J. L. Walter, Evaluation of Directionally Solidified Eutectic Superalloys for Turbine Blade Applications, NASA Tech. Report #CR 135151, April 1978.
3. A. Lawley, Conference on In-Situ Composites-II, Edited by M. R. Jackson, J. L. Walter, F. D. Lemkey and R. W. Hertzberg, Xerox Individualized Publishing, Lexington, Mass., p. 451, 1976.
4. N. S. Stoloff, in Advances in Composite Materials, Edited by G. Piatti, Applied Science Publishers Ltd., London, p. 274, 1978.
5. M. J. Salkind, in Interfaces in Composites, ASTM STP #452, Am. Soc. Testing and Mats., Phila., p. 149, 1969.
6. T. H. Courtney, Thermal and Mechanical Stability in Finely Divided Structures, in New Developments and Applications in Composites, AIME, in press.
7. H. B. Smartt and T. H. Courtney, Met. Trans., 7A, 123, 1976.
8. H. E. Cline, Acta Met., 19, p. 481, 1971.
9. A. J. Ardell, Met. Trans., 3, p. 1395, 1972.
10. G. C. Weatherly and Y. G. Nakagawa, Scripta Met., 5, p. 777, 1971.
11. Y. G. Nakagawa and G. C. Weatherly, Acta Met., 20, p. 345, 1972.
12. M. Gell, See reference #1, p. 117.
13. E. M. Breinan, E. R. Thompson and F. D. Lemkey, Proceedings of the Conference on In-Situ Composites, National Materials Advisory Board, National Academy of Sciences, 1973, #308-I, p. 201.
14. F. M. Dunlevy and J. F. Wallace, Met. Trans. A, 1974, Vol. 5A, p. 1351.
15. J. L. Walter and H. E. Cline, see reference #13, p. 61.
16. E. R. Buchanan and L. A. Tarshis, Met. Trans., 4, p. 1895, 1973.
17. H. Bibring, see reference #13, p. 1.
18. D. A. Woodford, J. Materials Science and Engineering, 1976, Vol. 24, p. 257.
19. D. A. Woodford, see reference #3, p. 211.
20. D. A. Woodford, Met. Trans. A, 1977, Vol. 8A, p. 2016.
21. F. H. Harf and S. N. Tewari, Met. Trans. A, 1977, Vol. 8A, p. 202.
22. H. R. Gray and W. A. Sanders, see reference #3, p. 201.

23. E. R. Thompson and F. D. Lemkey, *Met. Trans.*, 1970, Vol. 1, p. 2799.
24. E. R. Thompson, D. A. Koss and J. C. Chesnutt, *Met. Trans.*, 1970, Vol. 1, p. 2807.
25. L. Y. Lin, M. H. Abdel Latif and A. Lawley, Proc. Second Int. Conference on Composite Materials, AIME, Editors: B. R. Noton, R. Signorelli, K. Street and L. Phillips, 1978, p. 770.
26. M. H. Abdel Latif and A. Lawley, "Effect of Thermal Treatment on the Structure and Toughness of the Co,Cr-(Cr,Co)₇C₃ In-Situ Composite", ONR Technical Report (Contract #N00014-76-C-0205) Drexel University, Phila., Pa., December 1978.
27. M. H. Abdel Latif and A. Lawley, "Fatigue Crack Propagation in a Co,Cr-(Cr,Co)₇C₃ Composite", ONR Technical Report (Contract #N00014-76-C-0205), Drexel University, Phila., Pa., December 1978.
28. E. R. Thompson, F. D. George and E. M. Breinan, Proceedings Conf. on In-Situ Composites, National Materials Advisory Board, National Academy of Sciences, 1973; #308, p. 71.
29. H. Saatchi, "Microstructural Stability and Strength of the Monovariant Co,Cr-(Cr,Co)₇C₃ Composite", June 1978, Ph.D. Thesis, Drexel University, Philadelphia, Pa.
30. V. W. Köster and H. Sperner, *Arch. Eisenhuettenw.*, 1955, Vol. 22, p. 555.
31. P. R. Sahm, M. Lorenz, W. Hugi and V. Fruhauf, *Met. Trans.*, 1972, Vol. 3, p. 1022.
32. A. J. Perry, A. R. Nicholl and P. R. Sahm, Brown Boveri Research Center, Baden, Switzerland, unpublished work, 1973.
33. B. Scarlin, *Met. Trans.*, 1977, Vol. 8A, p. 1941.
34. D. A. Koss and S. M. Copley, *Met. Trans.*, 1971, Vol. 2, p. 1557.
35. N. F. Dow, B. H. Rosen, L. S. Shu and C. H. Zweeken, "Design Criteria and Concepts for Fibrous Composite Structures", NASA Final Tech. Report #NASW-1377, July 1967.
36. E. R. Buchanan and L. A. Tarshis, *Met. Trans.*, 1974, Vol. 5, p. 1413.
37. M. F. Ashby, Proc. Second Bolton Landing Conference on Oxide-Dispersion Strengthening, Gordon and Breach, N.Y., 1968.
38. E. O. Hall, *Proc. Phys. Soc.*, 1951, Vol. 64B, p. 747.
39. N. J. Petch, *J. Iron and Steel Inst.*, 1953, Vol. 173, p. 25.
40. Y. Taniyama and A. Lawley, "Elevated Temperature Stability of a Co-Cr-C In-Situ Composite", Proceedings Conference on In-Situ Composites-III, Boston, Mass., November 1978, in press.

TABLE I. Effect of Isothermal Exposure and Thermal Cycling on Microstructure and Strength

I. Isothermal Exposure	Time	Phase Present	Strength	Changes in Microstructure
913°C	Up to 4.41×10^6 s	$\gamma(\text{Co}) + K'_2 + K'_3$	Increases then Decreases	<ul style="list-style-type: none"> • Precipitation • Spheroidization of Precipitate • Splitting of Fibers • Rounding of Fibers
1121°C	Up to 4.41×10^6 s	$\gamma(\text{Co}) + K'_2$	Small Increase	<ul style="list-style-type: none"> • Splitting of Fibers • Rounding of Fibers
1242°C	Up to 3.6×10^5 s	$\gamma(\text{Co}) + K'_2$	Not determined	<ul style="list-style-type: none"> • Splitting of Fibers • Rounding of Fibers
913°C then 1121°C	4.41×10^6 s plus 4.5×10^5 s	$\gamma(\text{Co}) + K'_2 + K'_3$ then $\gamma(\text{Co}) + K'_3$	Increases then Decreases	<ul style="list-style-type: none"> • Precipitation/Dissolution • Splitting of Fibers • Spheroidization of Fibers
II. Thermal Cycling				
357°C to 913°C	0	$\gamma(\text{Co}) + K'_2 + K'_3$	Increases with # of cycles	<ul style="list-style-type: none"> • Precipitation • Spheroidization of Precipitate • Rounding of Fibers
538°C to 1121°C	0	$\gamma(\text{Co}) + K'_2 + K'_3$	Increases with # of cycles	<ul style="list-style-type: none"> • Precipitation/Dissolution • Rounding of Fibers • Spheroidization of Precipitate • Splitting of Fibers
746°C to 913°C	480s at T_{max} and T_{min}	$\gamma(\text{Co}) + K'_2 + K'_3$	Increases with # of cycles	<ul style="list-style-type: none"> • Precipitation • Spheroidization of Precipitate • Splitting of Fibers • Rounding of Fibers
538°C to 1121°C	3.3×10^3 s at T_{max}	$\gamma(\text{Co}) + K'_2$	Increases then decreases with # of cycles	<ul style="list-style-type: none"> • Precipitation/Dissolution • Splitting of Fibers • Spheroidization of Fibers • Void Formation

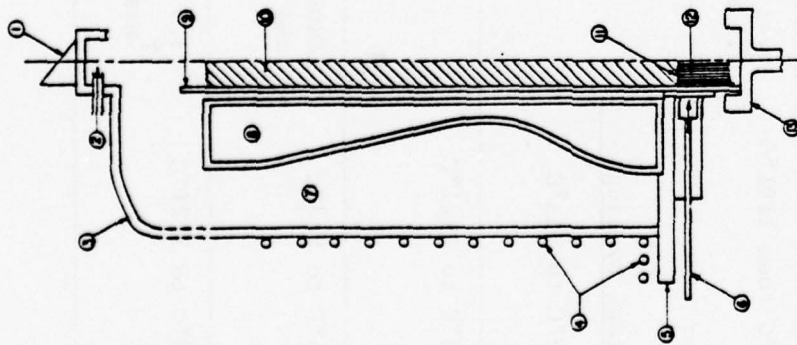
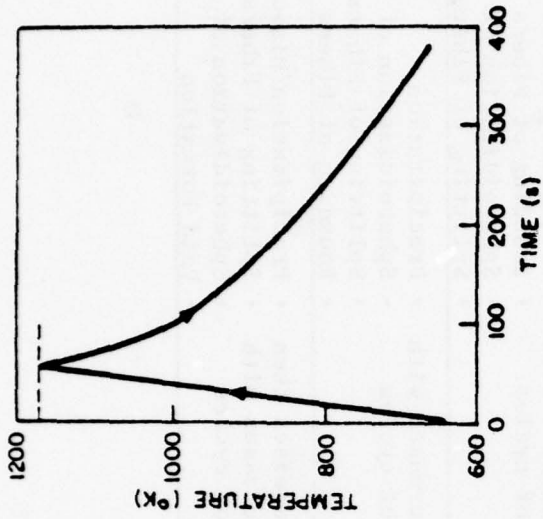
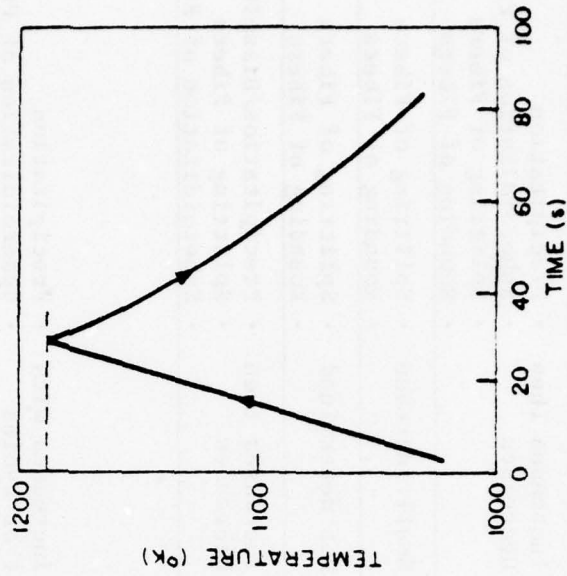


Figure 1. Schematic of facility for directional solidification of composites: (1) viewing prism; (2) argon in; (3) pyrex outer chamber; (4) induction coils; (5) ceramic insulator; (6) water spray; (7) graphite felt; (8) graphite susceptor; (9) alumina tube, (10) liquid alloy; (11) solid-liquid interface; (12) solid composite; (13) movable pedestal.



(a)



(b)

Figure 2. Heating and cooling profiles for thermal cycling. (a) 357°C to 913°C; (b) 746°C to 913°C.

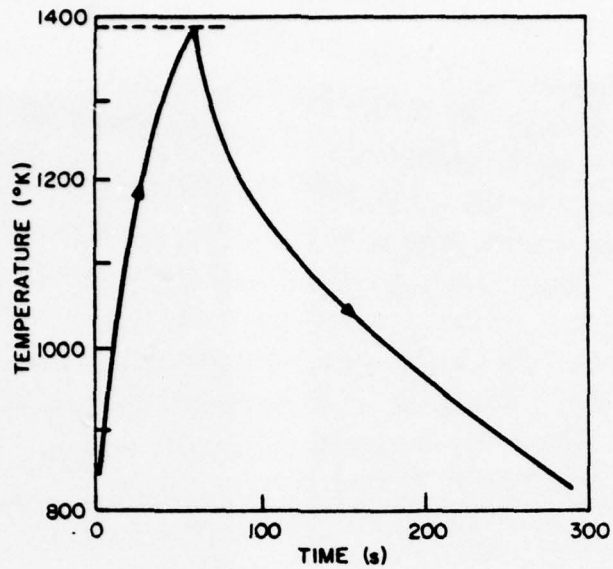


Figure 3. Heating and cooling profile for thermal cycling between 538°C and 1121°C.

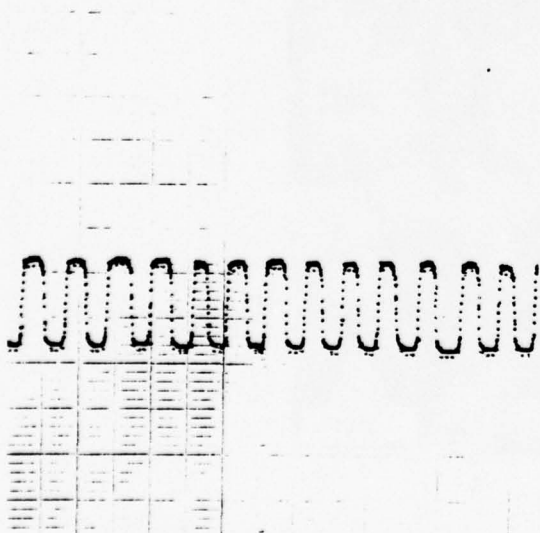
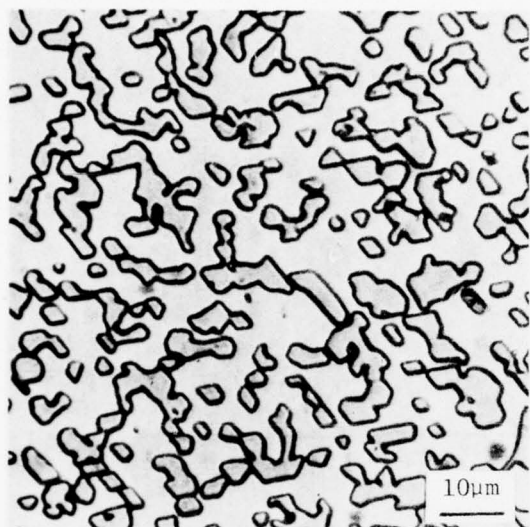


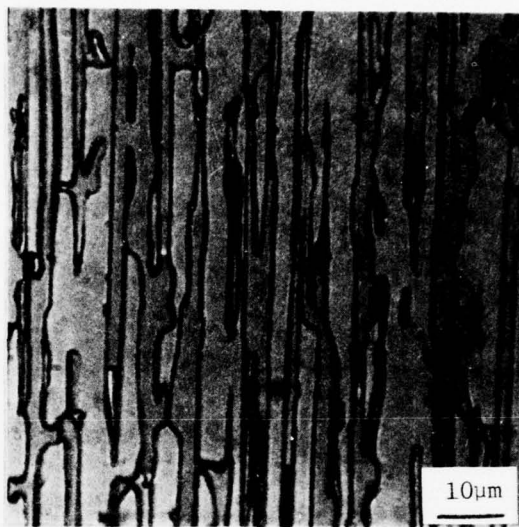
Figure 4. Heating and cooling profiles; thermal cycling between 746°C and 913°C with 480s hold time at T_{max} and T_{min} .



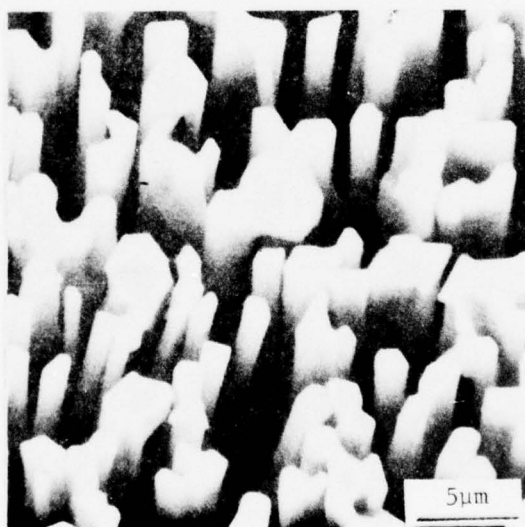
Figure 5. Heating and cooling profiles; thermal cycling between 538°C and 1121°C with 3360s hold time at T_{max} .



(a)

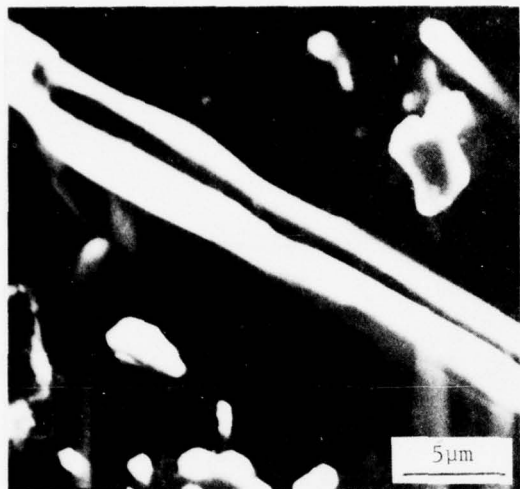


(b)

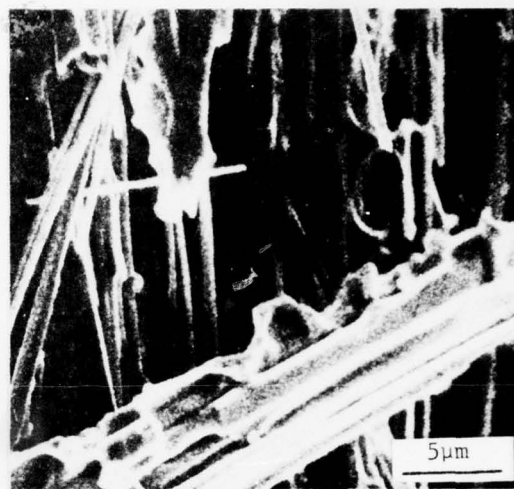


(c)

Figure 6. (a) Transverse, (b) longitudinal section optical micrographs and (c) SEM of as-grown composite.



(a)



(b)

Figure 7. SEM of fibers extracted from as-grown composite.



Figure 8. TEM of fiber extracted from as-grown composite showing side branches.

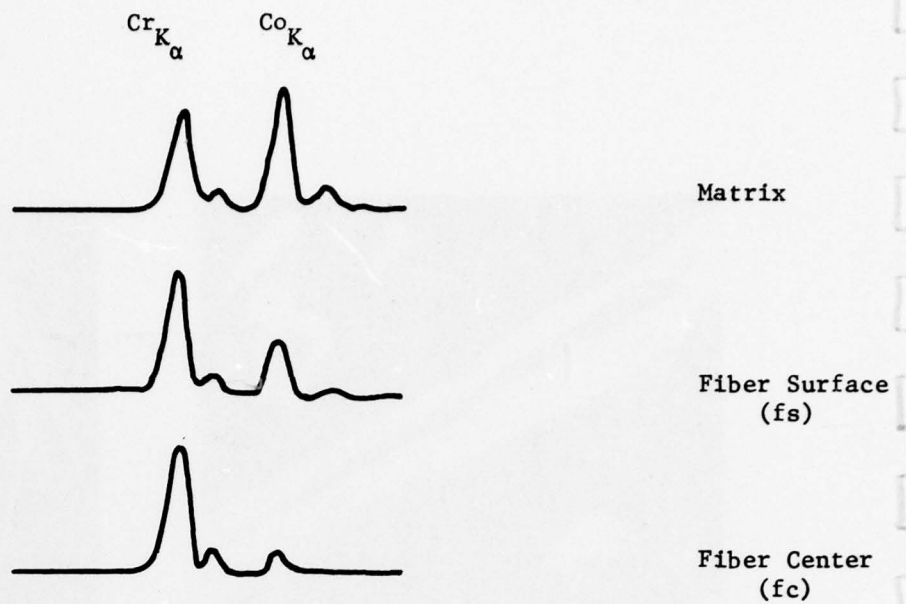


Figure 9. Energy-dispersive x-ray point analysis of as-grown composite.

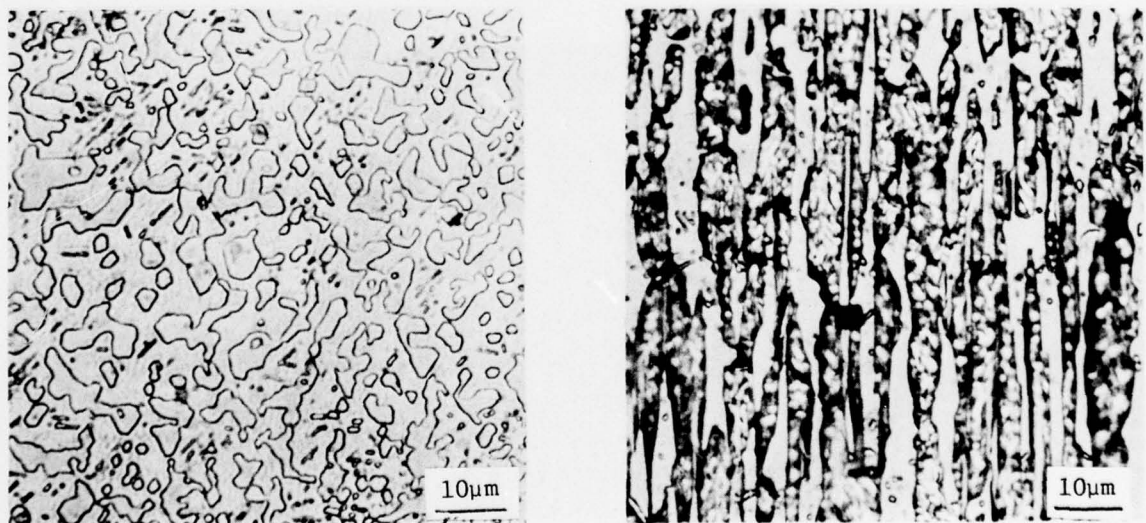


Figure 10 (a) Optical micrographs of transverse and longitudinal sections after 1.44×10^6 s at 913°C .

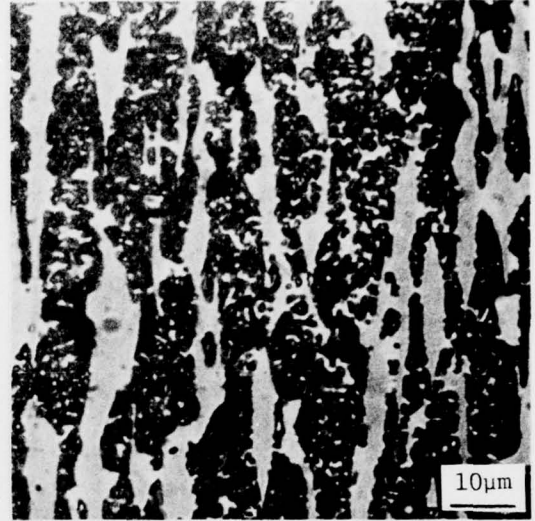
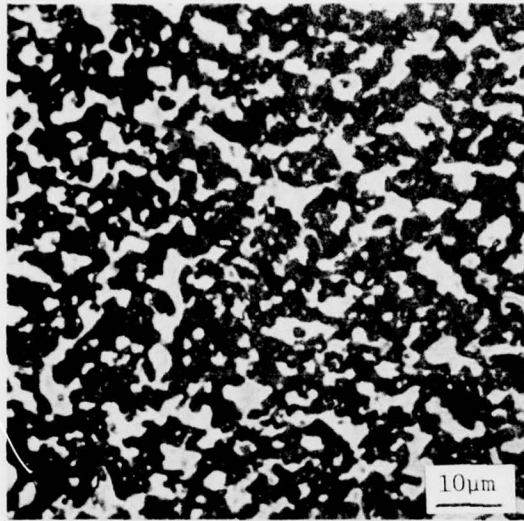


Figure 10(b) Optical micrographs of transverse and longitudinal sections after 2.88×10^6 s at 913°C .

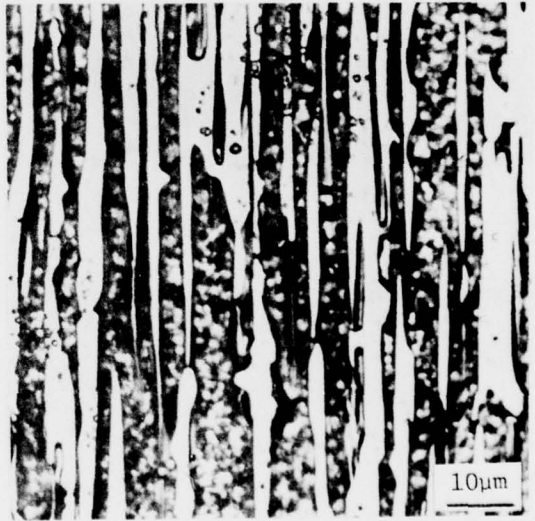
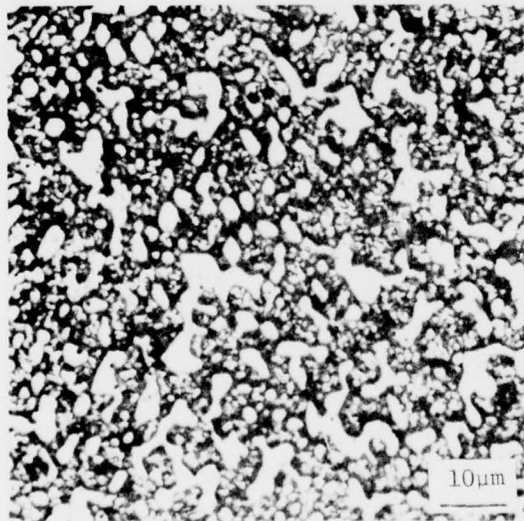


Figure 10(c) Optical micrographs of transverse and longitudinal sections after 4.41×10^6 s at 913°C .

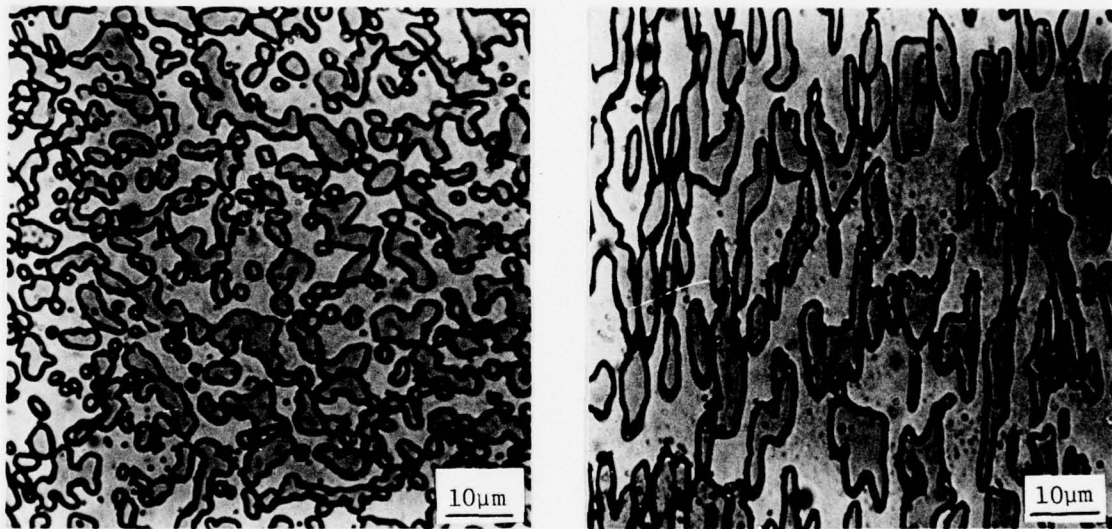
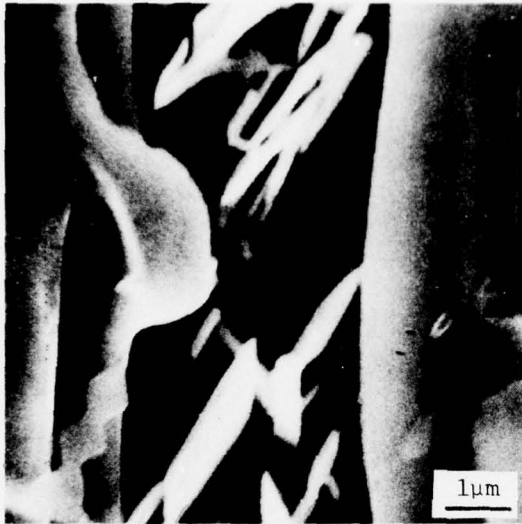
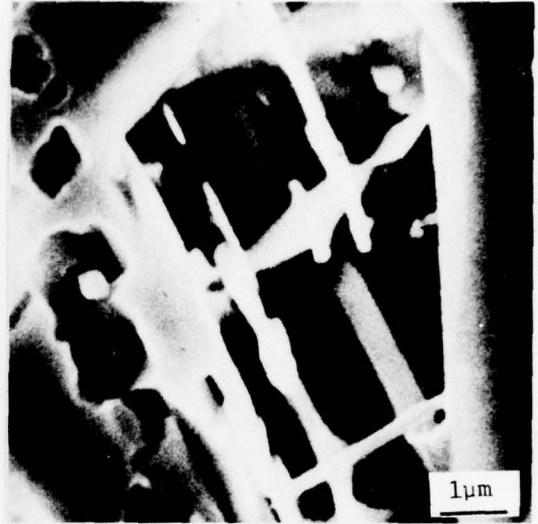


Figure 10(d) Optical micrographs of transverse and longitudinal sections after 4.41×10^6 s at 913°C plus 6.3×10^4 s at 1121°C .



(a)



(b)



(c)

Figure 11. SEM showing precipitates in the matrix between fibers after exposure at 913°C; (a) 1.44×10^6 s, (b) 2.88×10^6 s, (c) 4.41×10^6 s.

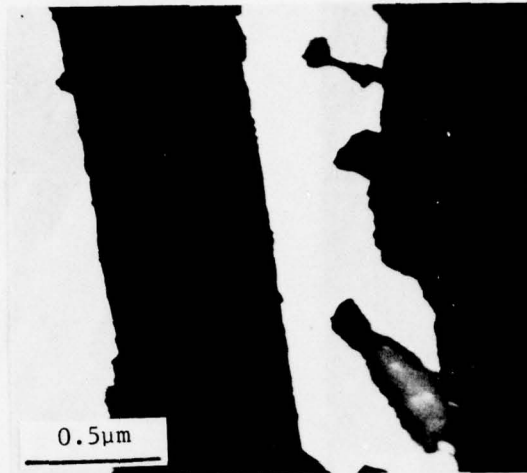


Figure 12. TEM showing fiber morphology after exposure of composite for 4.41×10^6 s at 913°C .

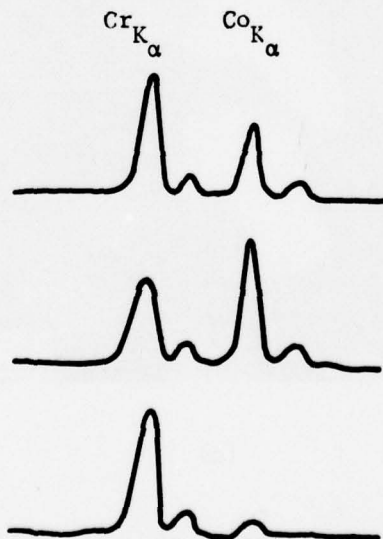


Figure 13. Energy-dispersive x-ray point analysis of composite after 2.88×10^6 s at 913°C .

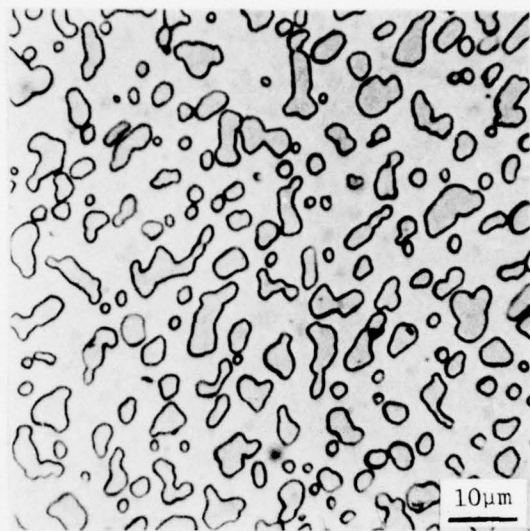
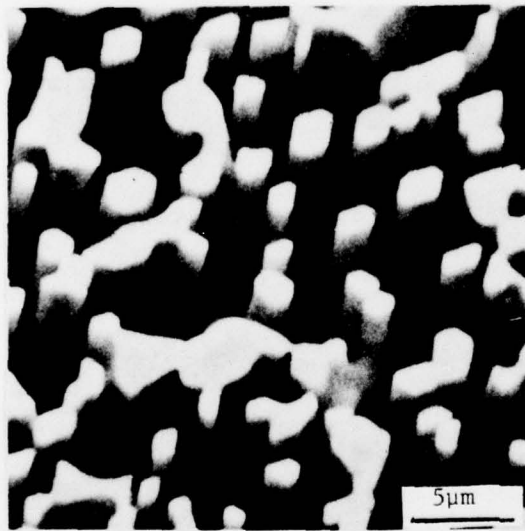
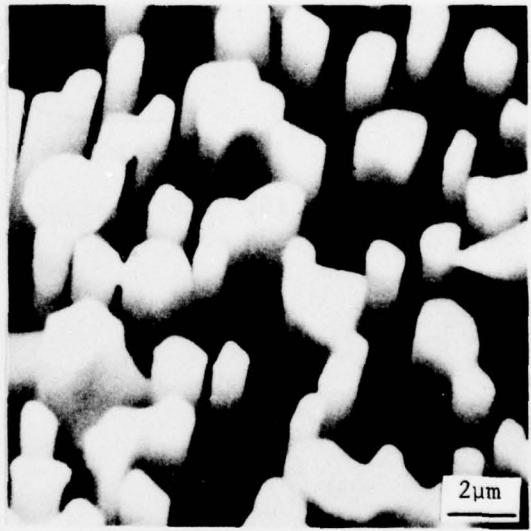


Figure 14. Transverse orientation optical micrograph after 3.6×10^5 s at 1242°C .



(a)



(b)

Figure 15. Scanning electron micrographs of composites after exposure at 1121°C ; deep etched. (a) 2.7×10^6 s, (b) 3.3×10^6 s.

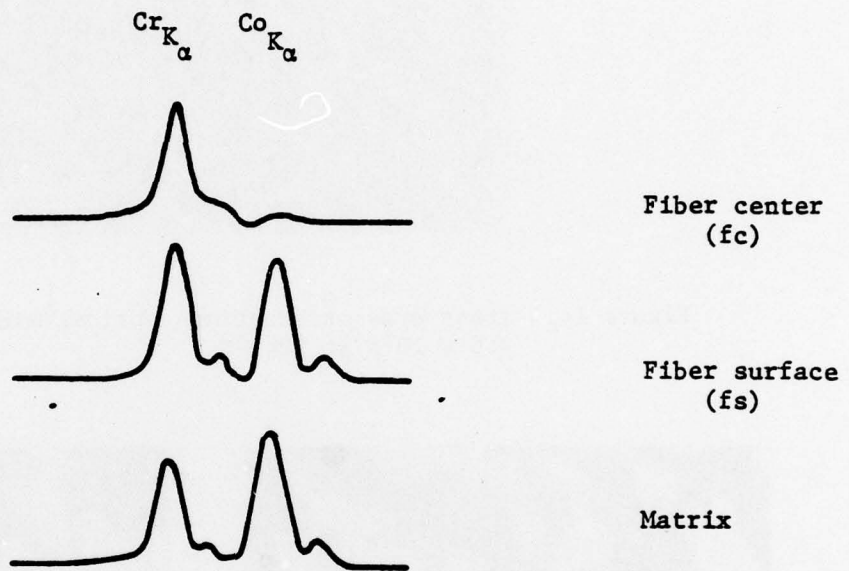
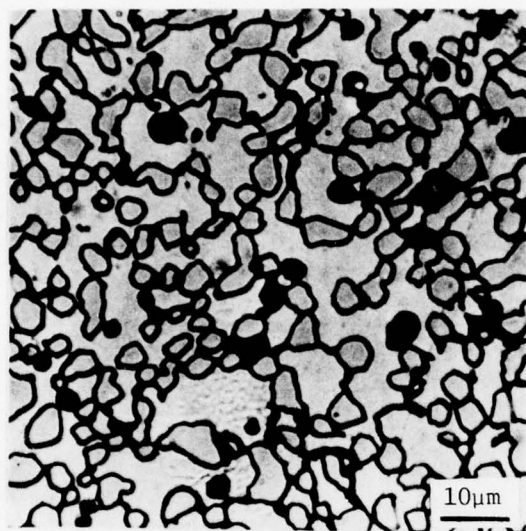
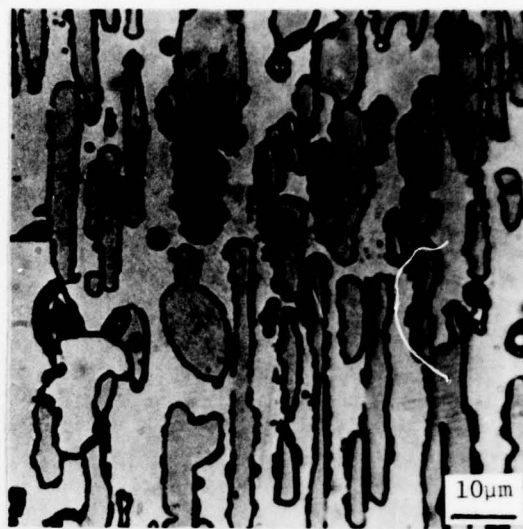


Figure 16. Energy-dispersive x-ray point analysis of composite after 3.6×10^5 s at 1242°C .



(a)



(b)

Figure 21. Optical micrographs after 1000 cycles between 538°C and 1121°C with a 3360s hold time at T_{\max} . (a) Transverse, (b) longitudinal sections.

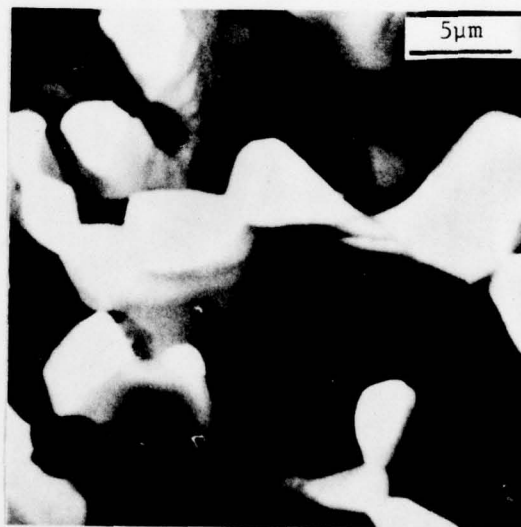
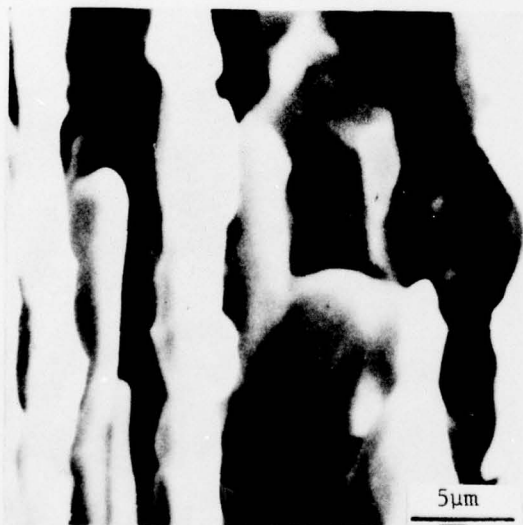


Figure 22. SEM after 1000 cycles between 538°C and 1121°C with a 3360s hold time at T_{\max} ; deep matrix etch.

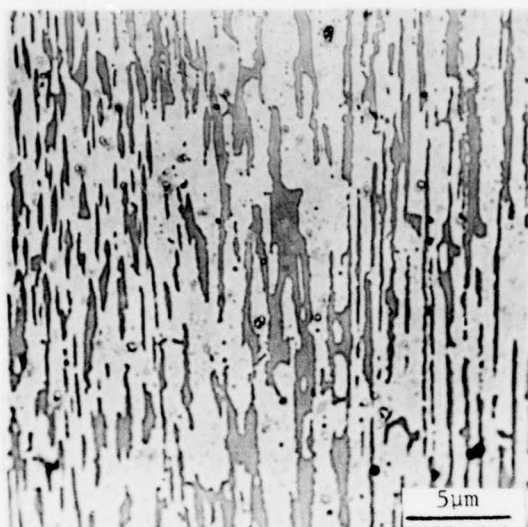


Figure 17. Longitudinal section optical micrograph; 3000 cycles between 357°C and 913°C.

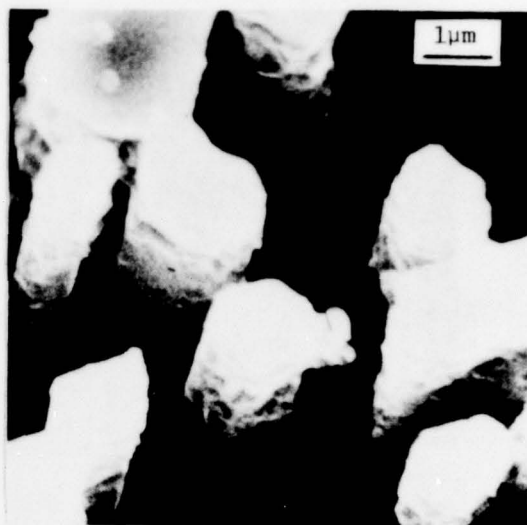


Figure 18. SEM after 7000 cycles between 357°C and 913°C; deep matrix etch.

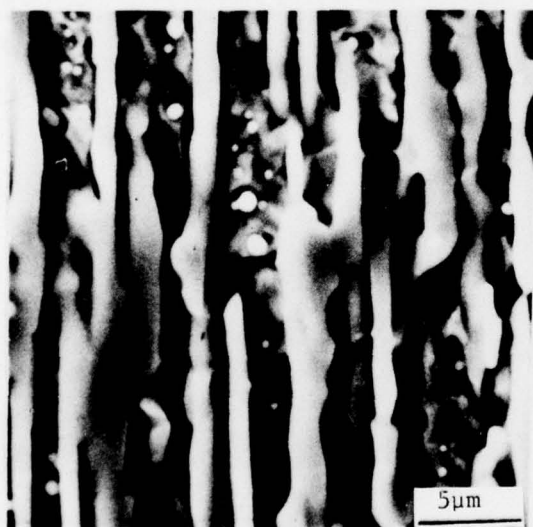


Figure 19. SEM after 1000 cycles between 746°C and 913°C with 480s hold time at T_{max} and T_{min} .

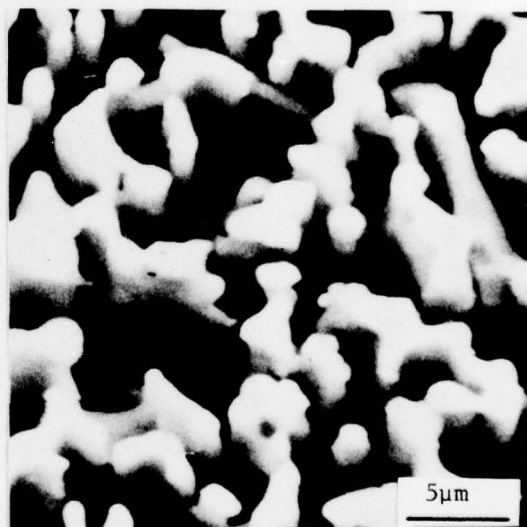


Figure 20. SEM after 1000 cycles between 746°C and 913°C with 480s hold time at T_{max} and T_{min} ; deep matrix etch.

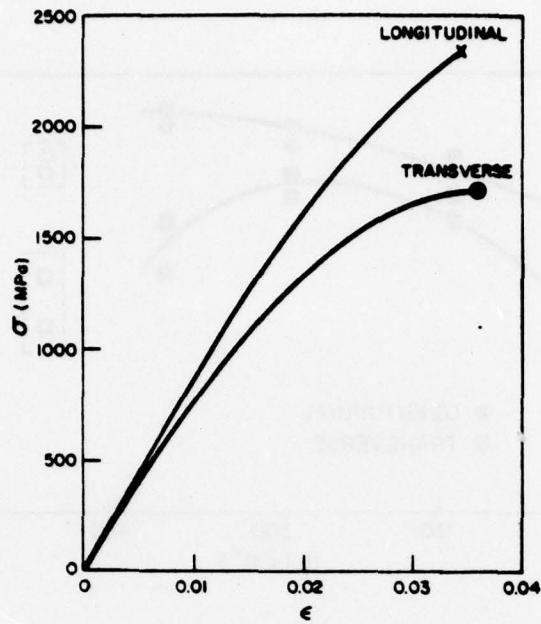


Figure 23. Compressive engineering stress-engineering strain curves at room temperature.

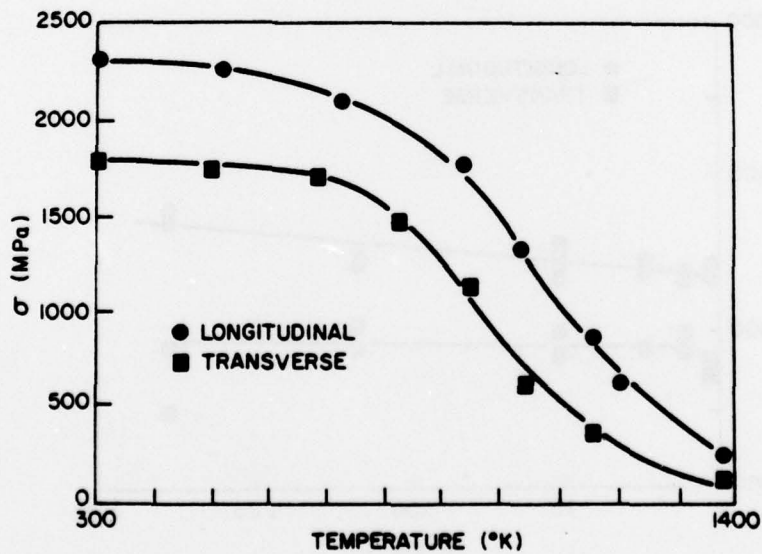


Figure 24. Ultimate compressive strength as a function of temperature.

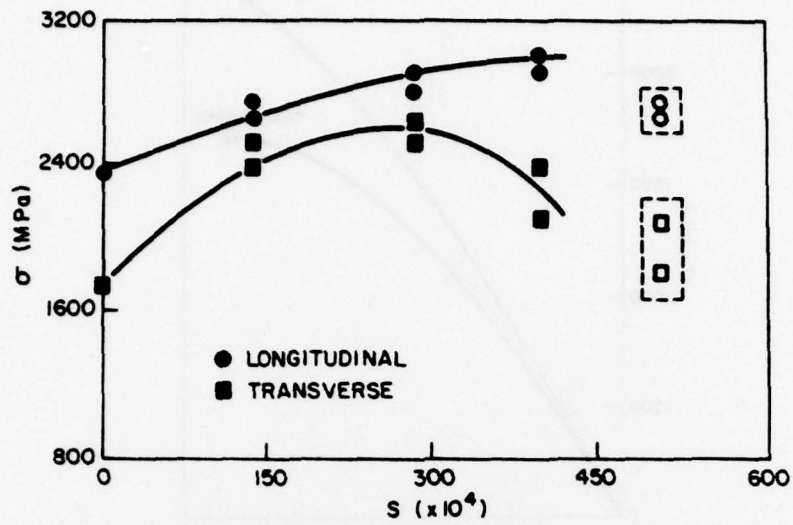


Figure 25. Ultimate compressive strength as a function of exposure time at 913°C .

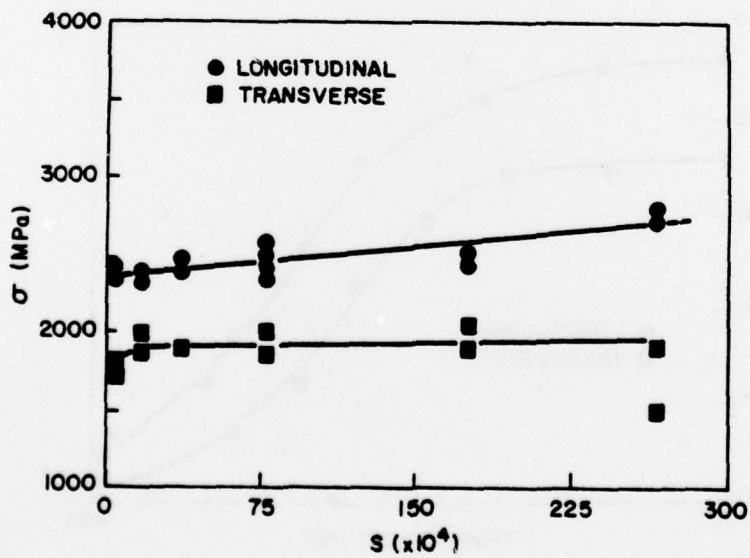


Figure 26. Ultimate compressive strength as a function of exposure time at 1121°C .

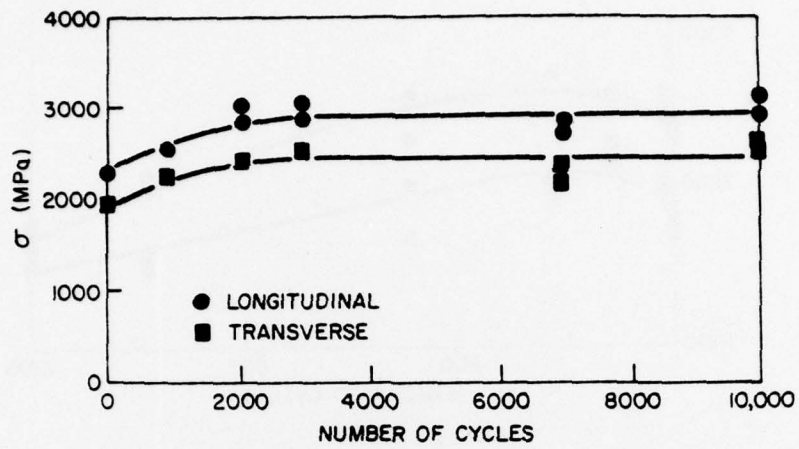


Figure 27. Ultimate compressive strength as a function of thermal cycling between 357°C and 913°C.

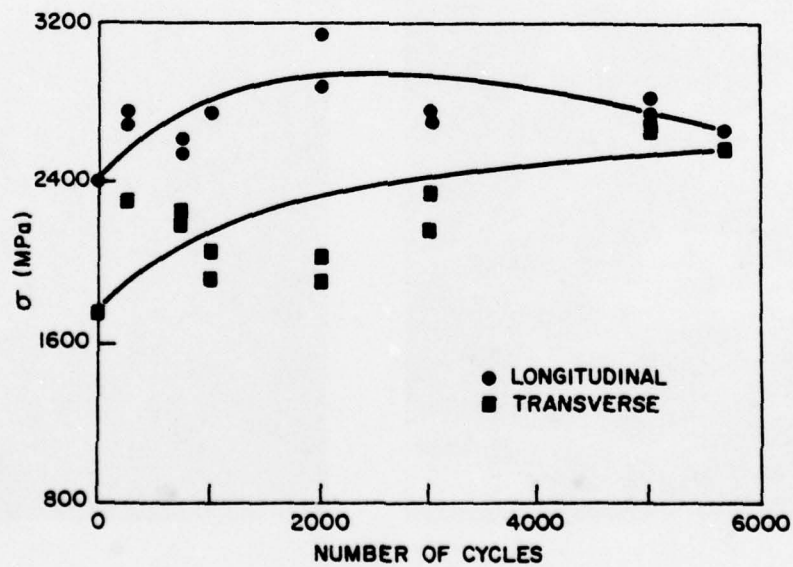


Figure 28. Ultimate compressive strength as a function of thermal cycling between 538°C and 1121°C.

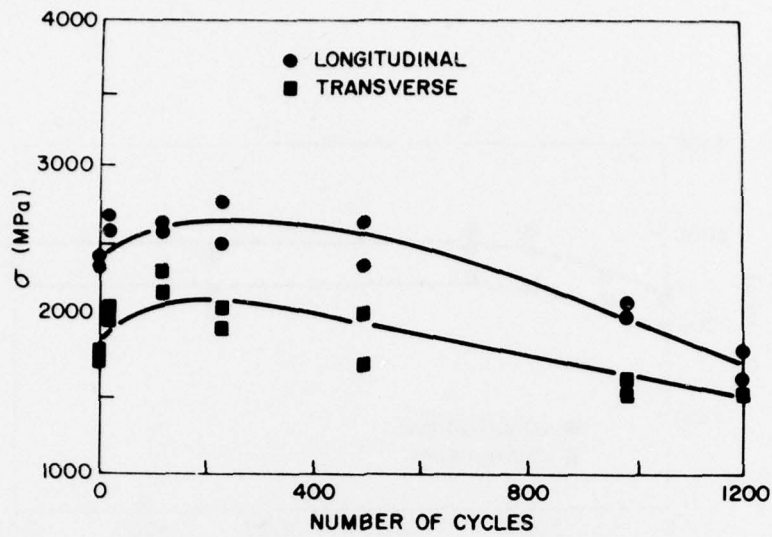
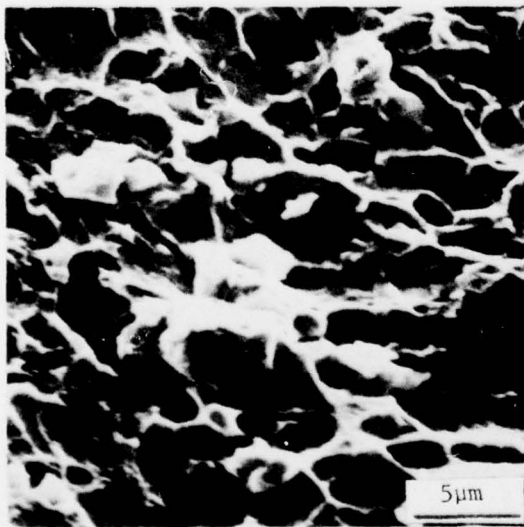


Figure 29. Ultimate compressive strength as a function of thermal cycling between 538°C and 1121°C with a 3300s hold time at T_{max} .

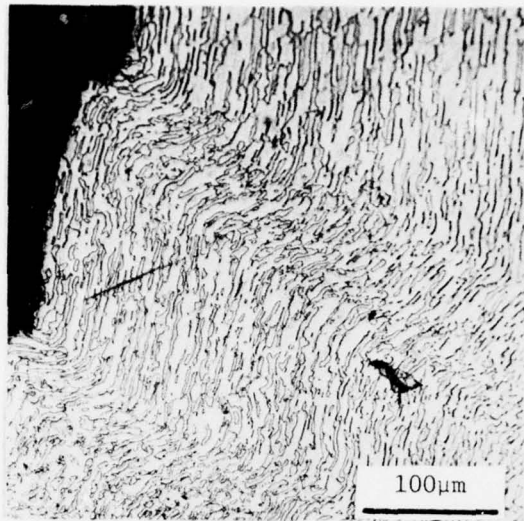


(a)

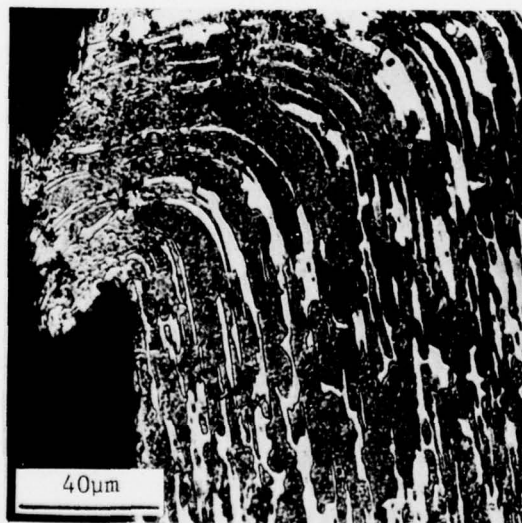


(b)

Figure 30. SEM of transverse orientation fracture surfaces after compressive loading to failure at room temperature. (a) matrix shearing/dimples, 10^4 cycles between 357°C and 913°C; (b) transverse fiber cleavage, isothermal exposure at 1121°C.



(a)



(b)

Figure 31. Compressive deformation (longitudinal orientation) at 929°C.
(a) as-grown; (b) after thermal cycling.

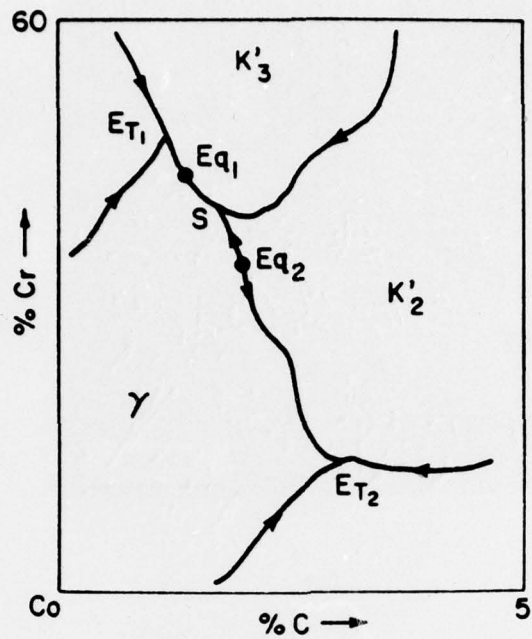


Figure 32. Liquidus surface in the cobalt rich corner of the Co-Cr-C System (23,30).

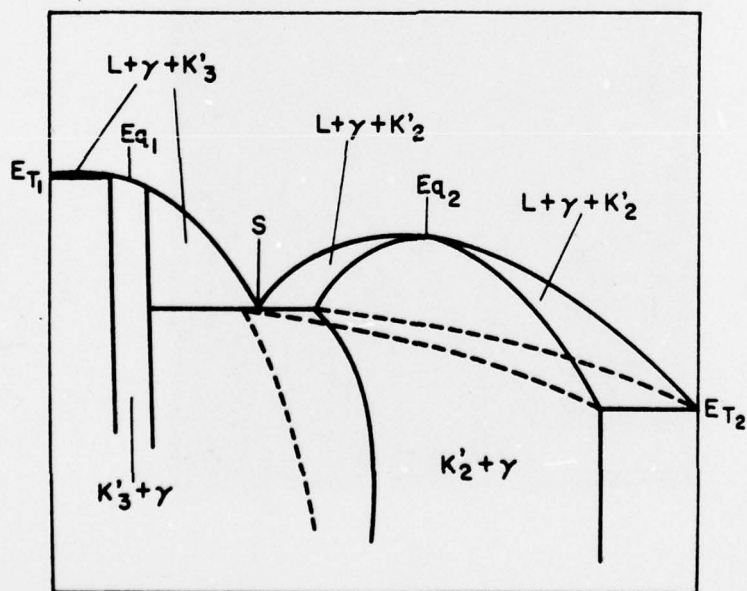


Figure 33. Section along eutectic trough in the Co-Cr-C System (30,31).

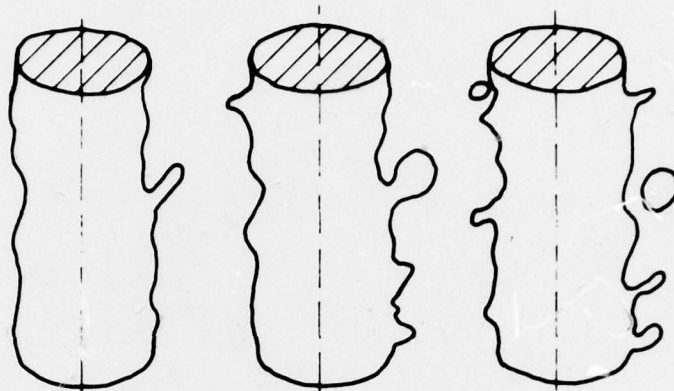


Figure 34. Schematic to illustrate sequence involved in the formation of the K_3' carbide precipitate from the main K_2' carbide fiber.

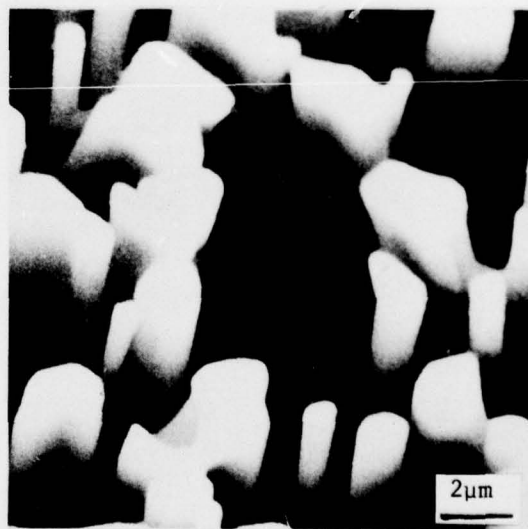
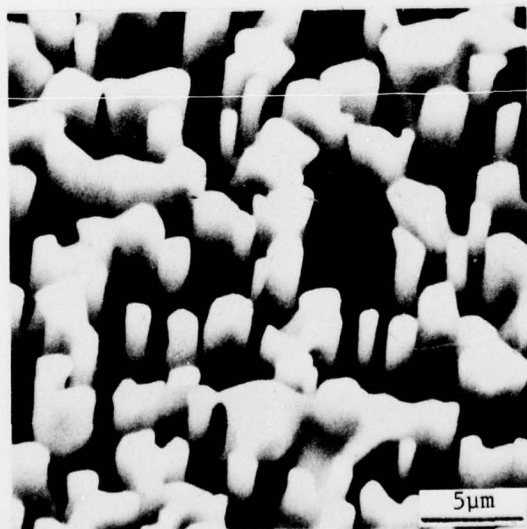


Figure 35. Scanning electron micrographs after thermal cycling between 538°C and 1121°C; 250 cycles, deep matrix etch.

Unclassified

SECURITY CLASSIFICATION OF THIS PAGE (When Data Entered)

REPORT DOCUMENTATION PAGE		READ INSTRUCTIONS BEFORE COMPLETING FORM
1. REPORT NUMBER	2. GOVT ACCESSION NO.	3. RECIPIENT'S CATALOG NUMBER
4. TITLE (and Subtitle) MICROSTRUCTURAL STABILITY AND STRENGTH OF THE Co,Cr-(Cr,Co) ₇ C ₃ IN-SITU COMPOSITE.		5. TYPE OF REPORT & PERIOD COVERED Final Report, March 1979
7. AUTHOR(s) H. Saatchi and A. Lawley		6. PERFORMING ORG. REPORT NUMBER
9. PERFORMING ORGANIZATION NAME AND ADDRESS Department of Materials Engineering Drexel University Philadelphia, Pa. 19104		8. CONTRACT OR GRANT NUMBER(s) N00014-76-C-0205
11. CONTROLLING OFFICE NAME AND ADDRESS Office of Naval Research Arlington, Virginia 22217		10. PROGRAM ELEMENT, PROJECT, TASK AREA & WORK UNIT NUMBERS
14. MONITORING AGENCY NAME & ADDRESS (if different from Controlling Office) 12 44p.		12. REPORT DATE Mar 1979
		13. NUMBER OF PAGES 34
		15. SECURITY CLASS. (of this report) Unclassified
		15a. DECLASSIFICATION/DOWNGRADING SCHEDULE
16. DISTRIBUTION STATEMENT (of this Report) Unlimited		
17. DISTRIBUTION STATEMENT (of the abstract entered in Block 20, if different from Report)		
18. SUPPLEMENTARY NOTES		
19. KEY WORDS (Continue on reverse side if necessary and identify by block number) Metal matrix composites, directional solidification, thermal cycling, isothermal exposure, microstructure, strength, fracture		
20. ABSTRACT (Continue on reverse side if necessary and identify by block number) The effect of elevated temperature isothermal exposure and thermal cycling on microstructural stability and compressive strength of the in-situ rod-like composite Co,Cr-(Cr,Co) ₇ C ₃ ($V_f \approx 0.3$) has been examined. Microstructures were characterized by optical and electron metallography, x-ray point analysis and electron diffraction. Strength was evaluated in compression at ambient and elevated temperatures. Changes in microstructure with post-solidification treatments are shown to arise from a combination of precipitation and dissolution of (Co,Cr) ₂₃ C ₆ , rounding and splitting of the primary (Co,Cr) ₇ C ₃		

DD FORM 1 JAN 73 1473

EDITION OF 1 NOV 65 IS OBSOLETE
S/N 0102-014-5601

Unclassified

SECURITY CLASSIFICATION OF THIS PAGE (When Data Entered)

409 592 Jul

20. Abstract (Continued)

fibers, spheroidization of constituents and void formation at fiber-matrix interfaces. The observed strength changes are analyzed in terms of a dispersion-hardening model. Failure in compression below the ductile to brittle transition temperature of the reinforcement occurs by shear in the matrix accompanied by transverse cleavage of the fibers. Above the ductile-to-brittle transition temperature of the reinforcing phase both matrix and carbide exhibit plastic flow.